Trapping crystallinity in highly crosslinked thermosets by light-based 3D printing from the liquid crystalline phase

Michael Göschl,[1] Dominik Laa,[2] Mojtaba Ahmadi,[2] Thomas Koch,[2] Jürgen Stampfl,[2] Katharina Ehrmann,[1,*] Robert Liska[1]

[1] Institute of Applied Synthetic Chemistry, Technische Universität Wien

[2] Institute of Materials Science and Technology, Technische Universität Wien

1 Abstract

We propel photopolymerizable liquid crystalline (LC) shape memory materials from solely elastomeric performance to the thermomechanical performance of tough, yielding thermosets. LC elastomers are at the forefront of smart, stimuli-responsive materials development. To apply their properties to mechanically superior thermosets, we demonstrate main-chain incorporation of high quantities of preordered LC motifs into a densely crosslinked network via thiol-ene photopolymerization to achieve a new material class hybridizing the advantages of LC elastomers and liquid crystalline networks. A terminal alkene mesogen with a robust LC phase is combined with multiple trithiol comonomers and selected based on resulting polymer crystallinities (13-37%). The bulk materials exhibit high strength, stiffness and pronounced yielding under stress with elongations around 200%. Their excellent thermomechanical properties were explained by phase separation observed in atomic force microscopy. Furthermore, we demonstrate shape memory of these materials with fast, near-perfect shape imprinting (99%) and recovery (97%) over at least 20 cycles, and their light-based 3D printing at high temperature.

2 Introduction

Liquid crystalline elastomers (LCEs) are lightly crosslinked polymer networks that show promise in multiple future-oriented industries like soft robotics,[1-3] electronics[4,5] and the medical industry[6-8] because they exhibit unique reversible mechanical,[9-11] optical,[12,13] electrical[14,15] and thermal[16-18] properties. One particularly outstanding feature is their ability to react to external stimuli, allowing modulation of mentioned properties on demand. These stimuli can be electricity,[15] light,[19,20] mechanical stress[21] or temperature changes triggering reversible shape deformation (actuation) up to 400%[22-28] or color/opacity changes.[21,29]

LCEs are typically produced by pre-polymerizing an LC monomer and a chain extender, followed by alignment through stretching, rubbed surfaces, 3D printing[30], or electrical or magnetic field exposure. The mesogenic groups may be located in the polymer backbone (main-chain LCE)[31] or as a pendant group (side-chain LCE).[32] After the alignment, a crosslinking step is employed, leading to a loosely crosslinked, elastomeric network with a well-defined structure. Thus, functional LCE materials are typically soft, elastic materials.[24,33,34]

Liquid crystalline networks (LCN), or liquid crystalline thermosets, are highly crosslinked polymer networks containing mesogenic groups. Their crosslinking densities, and thus their properties, are similar to conventional thermosets, which may be obtained by polymerizing e.g., (meth)acrylate monomers with a high fraction of crosslinker. By aligning the mesogens in LCNs before polymerization, directional anisotropy in mechanical properties, in particular high strength in the direction of the alignment, can be achieved. However, these highly crosslinked materials are usually frozen in their glassy state exhibiting low crystallinity and actuation strains below 5%.[24,35,36] Therefore, they are not suitable for use as smart materials in analogy to LCEs.

The combination of structured microphases with high crosslinking densities is arguably one of the leading challenges in soft matter material design in general[37] and for photo-polymers and 3D printing of photopolymers in stereolithographic processes specifically.[38]

Mastering this challenge promises access to stiff, high load bearing materials with additional functionality such as shape memory.

Herein, we propel 3D printable liquid crystalline shape memory materials from solely elastomeric performance to the thermomechanical performance of tough, yielding thermosets by utilizing Hot Lithography, which allows light-based printing at temperatures up to 140 °C. For this purpose, we have designed a mesogenic terminal alkene monomer to achieve a broad temperature range of the LC phase, which is stable even in the presence of non-LC thiol comonomers (**Figure 1**). The LC phase stability of this monomer is screened in combination with a variety of trifunctional thiol comonomers, which vary in molecular weight and rigidity. Furthermore, the liquid crystalline behavior before polymerization and the thermomechanical behavior after polymerization is

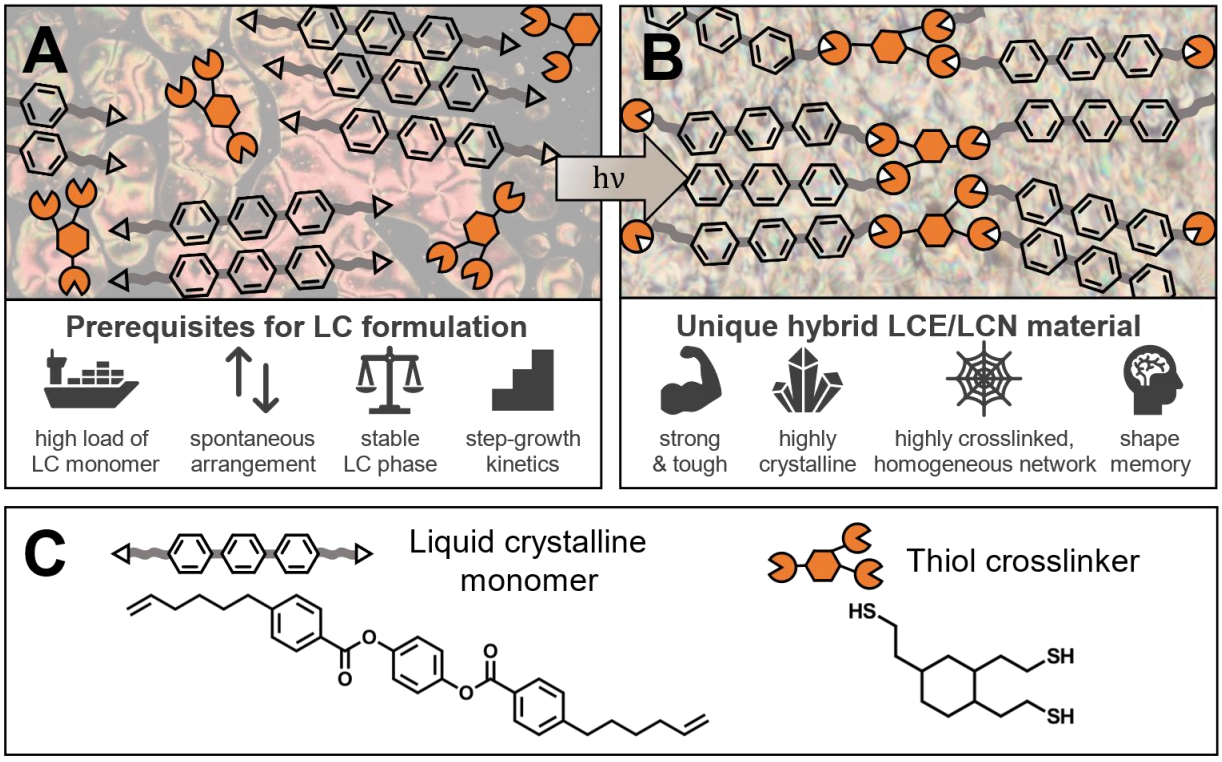

Figure 1: *Photopolymerization from the liquid crystalline phase.* ***A)*** *A photoreactive formulation comprising a liquid crystalline ene-monomer (LCM) and a low molecular weight trithiol crosslinker is heated above the monomers' collective melting point, where it exhibits a self-organized nematic liquid crystalline phase.* ***B)*** *Irradiation leads to a crosslinked, highly crystalline thermoset.* ***C)*** *Monomer combination, which leads to the highest polymer crystallinity.*

characterized. To confirm the hypothesized structure-property relationships, we elucidate the microstructure of the most crystalline materials. Finally, we successfully demonstrate shape-memory behavior and 3D printing for one monomer combination.

3 Liquid crystalline monomer design

As the key building block for highly crosslinked, crystalline polymer networks, we synthesized a novel difunctional liquid crystalline terminal alkene monomer (LCM, **Scheme 1**). We employ short six-carbon spacer chains to reach a high crosslinking density even with thiol-ene step growth polymerization. A manageable melting point (104 °C) allows processing and 3D printing and is achieved by avoiding a conventional aromatic ether bridge between mesogen and spacer. Instead, a cross-coupling reaction[39] attaches the spacer directly to the core, which we found to reduce the melting point.[40-42] A fully rod-shaped mesogenic core without side groups[43] ensures a broad LC phase (104-172 °C, Supplementary Figure 9), which is particularly important for consistent curing within the LC phase, since adding a non-LC thiol comonomer will reduce the LC temperature range. The type of liquid crystallinity for pure LCM was determined to be nematic by X-ray characterization (Supplementary Figure 11). This aligns with the Schlieren patterns observed via polarized optical microscopy (Supplementary Figure 10).

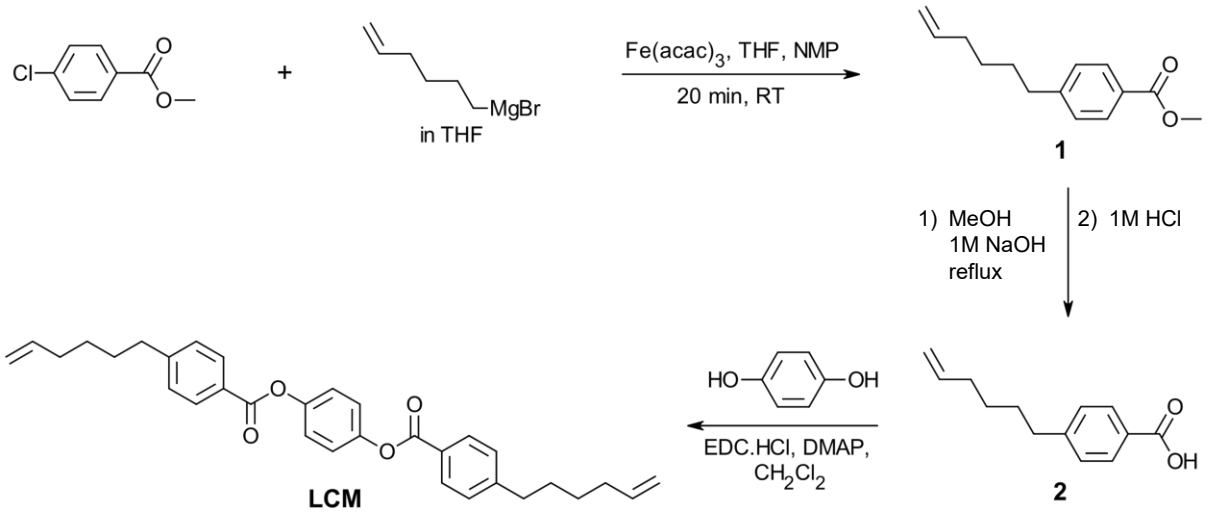

Scheme 1: *Synthesis of liquid crystalline terminal alkene monomer LCM.*

4 Comonomer selection

For optimal thermomechanical and shape memory performance, crystalline domains should be distributed homogeneously throughout the polymer network and exhibit narrow domain size distribution. Both are supported best by a thiol-ene radical addition reaction mechanism. Since the aliphatic terminal alkene group cannot homopolymerize,[44] an even distribution of mesogenic groups along the main chains is ensured.

The newly synthesized monomer was copolymerized with four different trifunctional thiol comonomers in photoreactive formulations (**Figure 2 A**), in which equal amounts of thiol and alkene groups were employed. To improve crystallinity, the mesogen load was maximized by avoiding dithiol chain extenders. Their liquid crystalline phase behavior was assessed on a polarized optical microscope and revealed a strong correlation of the weight fraction of LCM with the presence and stability of an LC phase (**Figure 2 B-D**). At nearly equal weight fractions of LCM and thiol in formulations containing 100% of the high-molecular weight comonomer ETTMP, no LC phase is observed. Mixtures of LCM with the comonomer TEMPIC increase the LCM weight fraction only slightly, hence an isotropic melt occurs across all temperature ranges, except for traces of liquid crystallinity close to the recrystallization temperature during cooling. The formulation containing TMPMP as comonomer displays a partial LC phase (less than 50% of the observed area covered by liquid crystalline regions, in the shape of small droplets), which persists for 25 °C above the melting point. From LCM weight fractions of at least 65% on, distinct LC phases dominate across large areas of the formulation, which is the case for the low-molecular weight crosslinker CHTT. To vary the crosslinking density, the flexible toughener ETTMP was added as substituent for CHTT in concentrations of 10 and 20 mol%, which did not cause a significant change of LC behavior. A stable LC phase across a temperature range of around 10 °C is formed by all three formulations, which gradually reduces in intensity before turning into a fully isotropic melt approximately 30 °C above the melting point. The exact weight fractions and phase transition temperatures are listed in the supplementary information (Supplementary Figure 14, Supplementary Table 1). Therein,

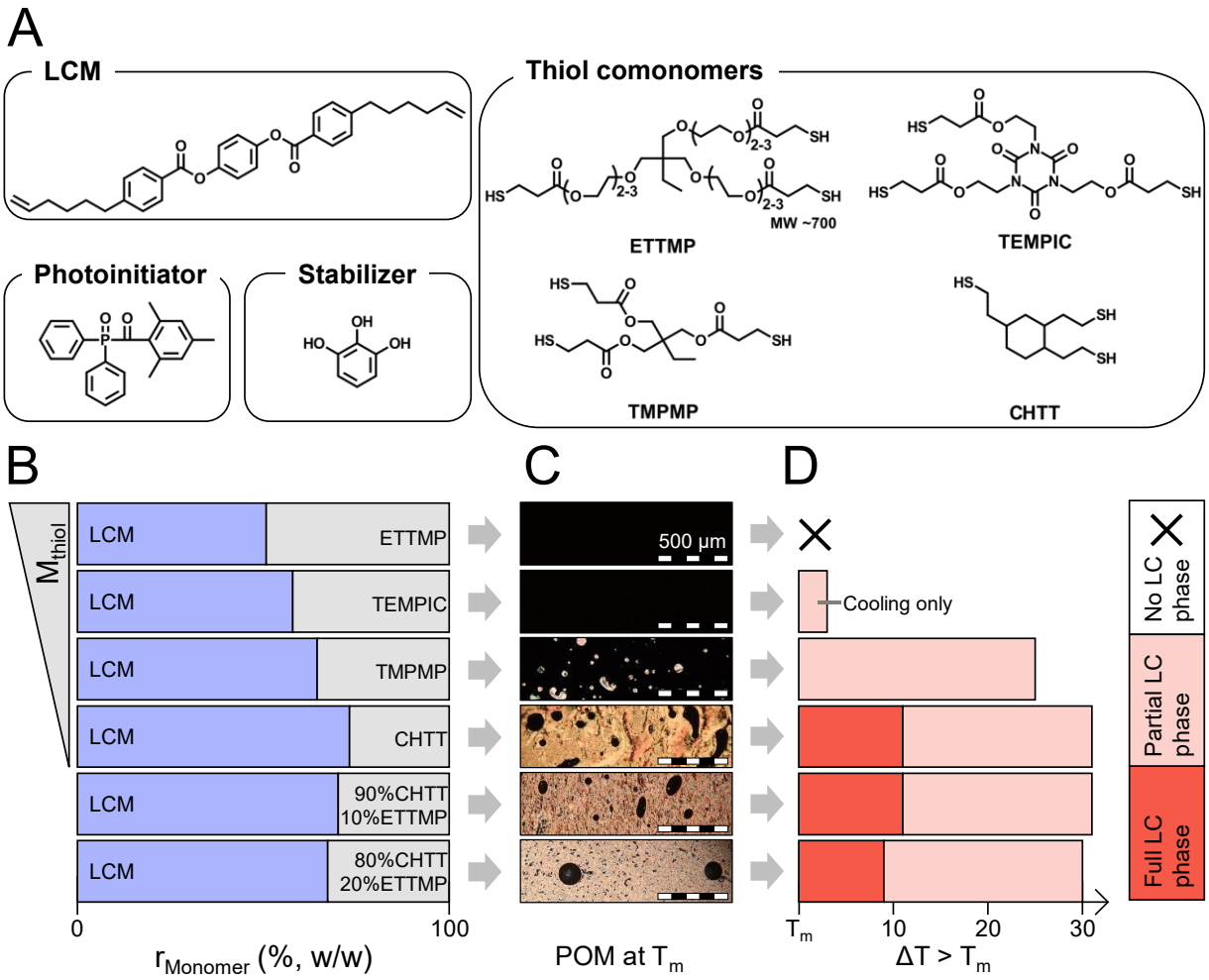

Figure 2: *Evaluation of liquid crystalline behavior of formulations.* ***A)*** *Components used in formulations: LCM, as the sole ene-component and sole LC-forming monomer, photoinitiator TPO (0.5 mol%), radical stabilizer pyrogallol (0.05 wt%), trithiol comonomers with different molecular weights (M_{thiol}).* ***B)*** *Weight ratios of LCM to thiol comonomers ($r_{Monomer}$) in formulations resulting from combinations of the monomers with equal stoichiometric amounts of terminal alkene and thiol groups.* ***C)*** *Polarized optical microscopy (POM) of formulations at their melting temperatures (T_m). Bright orange-brown areas are liquid crystalline, black areas are isotropic.* ***D)*** *Observations of LC phases in formulations at temperatures above the melting temperature ($\Delta T > T_m$). Liquid crystalline phases were considered as "partial" when at least 50% of the area observed during POM had turned into an isotropic melt.*

all recorded temperatures are subject to some interpretation (± 2-3 °C) as substance mixtures lead to more diffuse phase transitions compared to pure compounds.

To reproduce the formulations' liquid crystalline behavior during bulk polymerization, we designed a custom heated mold with precise temperature control (Supplementary Figures 1, 2). Furthermore, a customized curing protocol was established to avoid heating the

formulation above its liquid crystalline phase due to polymerization heat, initially employing a low-intensity irradiation step followed by a high intensity final curing step, which resulted in a soft, semitransparent specimen in the case of ETTMP, and in milky, opaque specimens in all other cases.

5 Crystallinity evaluation

To quantify the degree of crystallinity trapped in the semitransparent to opaque bulk specimens upon curing of the liquid crystalline formulations, the phase transitions of the samples were followed by differential scanning calorimetry (**Figure 3 A**).

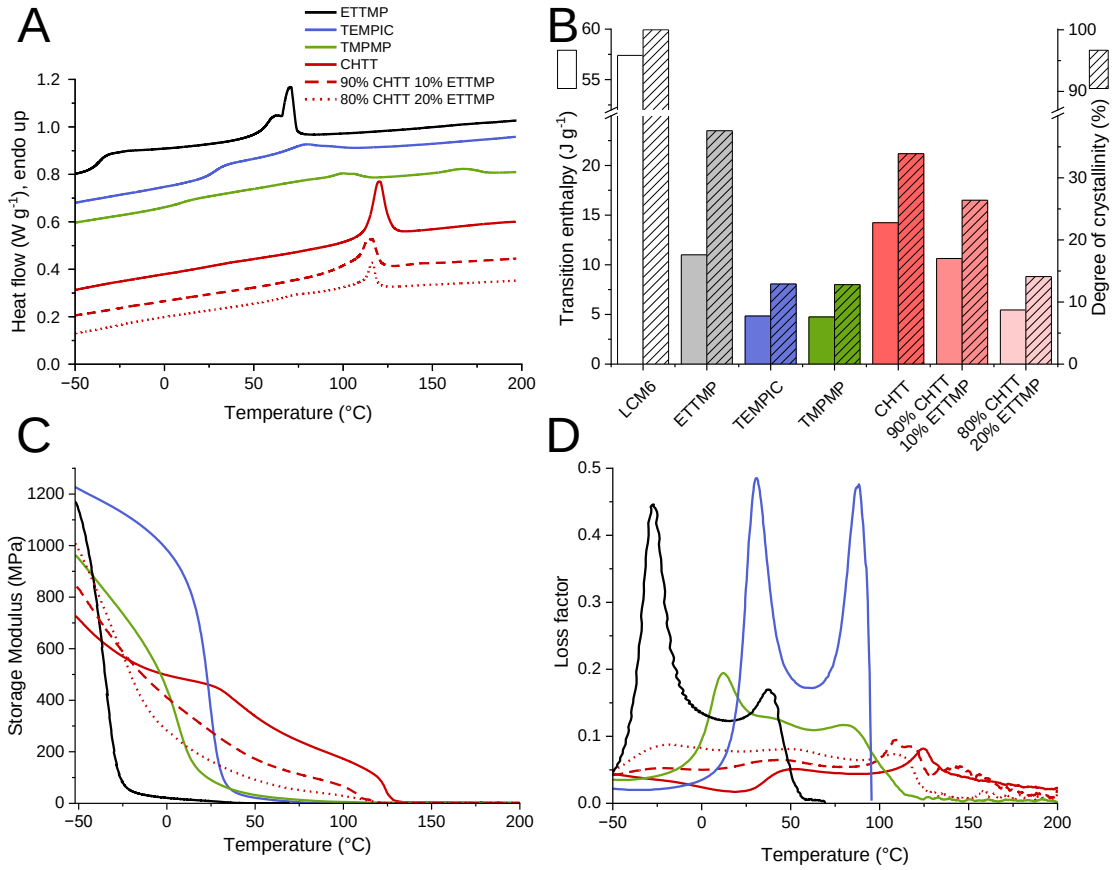

Figure 3: *Crystallinity analysis and thermomechanical behavior of liquid crystalline polymer networks obtained by polymerizing LCM with various trithiol monomers.* ***A)*** *Differential scanning calorimetry (DSC) measurements of polymers.* ***B)*** *Transition enthalpies obtained via integration of DSC signals and thereof calculated approximate polymer crystallinities according to supplementary equation 2.* ***C)*** *Storage modulus (G') and* ***D)*** *loss factor (tan δ) measured via dynamic mechanical analysis (DMA). An adjacent-averaging smoothing algorithm over 10 data points was applied for more effective analysis of loss factor curves.*

The networks comprising ETTMP, TEMPIC and TMPMP exhibit a visible glass transition temperature signified by an endothermal baseline shift, while no glass transition is observed when CHTT is used as a comonomer. Endothermal peaks signifying melting transitions confirm that we achieve crystallinity in all cases. To our knowledge, this was not achieved to date without the use of a chain extender in LC thiol-ene networks.[45-47] Very high crystallinity is achieved using pure ETTMP as comonomer, as well as CHTT with smaller amounts of ETTMP. Use of TEMPIC and TMPMP results in much lower crystallinity. We postulate two different mechanisms as the cause of crystallinity in the investigated samples. The presence of an LC phase before polymerization aids crystallization of the CHTT-containing polymers, while use of the flexible, long-chain comonomer ETTMP enables the liquid crystalline groups to crystallize spontaneously during or after polymerization akin to a more loosely crosslinked typical liquid crystalline elastomer. None of these two conditions are met for the TEMPIC- and TMPMP-containing specimens, which leads to their low crystallinity. The degree of crystallinity (**Figure 3 B**) is approximated based on the percentage of LCM in the formulation according to Supplementary Equation 2, which calculates the percentage of LCM that has crystallized in the polymer, assuming that the thiol comonomer does not contribute to crystallization. This approximation leads to LCM-ETTMP networks reaching the highest relative crystallinity while exhibiting the second highest melting transition enthalpy. This is closely followed by LCM-CHTT networks, which exhibit the highest melting transition enthalpy but lower relative crystallinity due to a lower comonomer molecular weight compared to LCM-ETTMP.

To determine whether crystallinity impacts the thermomechanical performance of bulk specimens, their storage moduli were determined as a function of temperature in dynamic mechanical analysis (DMA, **Figure 3C-D**). The storage modulus (G') of polymer networks typically decreases with increasing temperatures, signifying a transition from elastic towards more viscous behavior. Thereby, the slope of the curve is a material-specific parameter that varies depending on whether the network undergoes first a glass transition at lower temperatures, where short-range polymer chain motions become

accessible, and then a melting transition at higher temperatures, where the crystalline regions lose their long-range order. The change in slopes for the CHTT-containing specimens indicates that the crystallinity of these networks is particularly pronounced. Most intriguingly, crystallinity in CHTT-containing specimens shifts the decline of the storage modulus to higher temperatures, indicating a significant impact of crystallinity on the materials' thermomechanical behavior, which goes hand in hand with considerable enlargement of the application temperature window towards higher temperatures. For less crystalline samples, where the viscous behavior is more dominant, transitions in the loss factor, which is the ratio of loss to storage modulus, are more pronounced than changes in the storage modulus and hence convey the melting transition better. Its maxima signify the glass transition temperatures (T_g) and melting point (T_m). All glass transitions occur between -25 °C and room temperature, with higher T_gs for more rigid network structures due to shorter trithiol arms of the comonomer. Upon close examination of the curves, two glass transitions are visible if two trithiol comonomers are present in the polymer. Most interestingly, all networks exhibit maxima corresponding to the melting of crystalline domains, occuring at 38 °C for the loosest polymer network containing purely ETTMP as a comonomer, and above 80 °C for all other samples. This corroborates the DSC results that all networks exhibit a certain degree of crystallinity, whereby CHTT-containing networks have the most pronounced effect on the thermomechanical behavior. This is consistent with the determined degrees of crystallinity, with the exception of the network containing only ETTMP as comonomer. Even though this network is more crystalline, its loose network structure dissipates the stiffening effect that the crystalline domains should exhibit in the dominating rubbery matrix.

Early crystallization during polymerization could further cause an immobilization of reactive groups and thus affect the conversion of reactive groups in the different copolymer networks. Therefore, we determined reactive terminal alkene conversion via infrared spectroscopy, which was above 94% in all networks (Supplementary Figure 16). This indicates that the preordered state of the formulations aids homogeneous curing

regardless of crystallinity and does not inhibit complete reactive group conversion, which arguably sets these materials apart from other highly crystalline thermosets.

6 Mechanical and microstructural characterization

Due to the pronounced effects of crystallinity on the storage modulus observed in DMA and the excellent homogeneous and complete curing behavior of the bulk specimens, we anticipated excellent thermomechanical performance of these materials. Further tests exclude the comonomers TEMPIC and TMPMP as they result in a relatively unremarkable storage modulus progression and low crystallinity. Indeed, tensile tests reveal high tensile strength of around 19 MPa for the polymer employing pure CHTT as the comonomer (**Figure 4 A**). However, the high degree of crystallinity paired with a rigid network matrix causes brittle fracture at around 4% elongation. Conversely, using ETTMP as the exclusive comonomer results in a low tensile strength with a lower elongation at break than the specimen containing only 20% thiol end groups of ETTMP. When attempting to toughen the polymer by tuning the network density through substitution of CHTT with 10 mol% ETTMP, the tensile strength decreases but the elongation at break triples. Addition of 20 mol% ETTMP hardly affects the yield strength of the material compared to 10 mol% while massively improving the elongation at break to 200%. Together with the pronounced yield point and necking of the specimen, this photopolymer network remarkably resembles thermoplastic behavior.

To corroborate the assumption that crystallinity causes this shift in thermomechanical performance, we performed micro- and nanostructural characterization of the polymers. Polarized optical microscopy of 10 µm thick microtome cuts was performed, which reveals significant differences in the microstructure depending on the thiol crosslinkers incorporated into the polymer (**Figure 4 B**). Using pure CHTT as comonomer, a colorful Schlieren texture reminiscent of a nematic liquid crystalline phase is observed, leading to our interpretation of “trapping” the liquid crystalline phase. This effect is also observed when mixtures of CHTT and ETTMP are studied. However, the texture appears to be much more finely distributed, leading to a grainy multicolored appearance. Higher crystallinity

is identified through higher optical anisotropy in the purely CHTT-containing sample, which is signified by its lighter color under the crossed polarizers. With higher ETTMP-content, the color appears darker as crystallinity decreases. Pure ETTMP as comonomer leads to a spotted texture with alternating crystalline and amorphous areas. We postulate this large spherulite texture as the reason for the samples' subpar tensile properties. Potentially, a weakening effect occurs as the crystalline areas are not distributed homogenously enough throughout the bulk to achieve a stiff material. Therefore, when the material is strained, energy is solely absorbed by the amorphous regions.

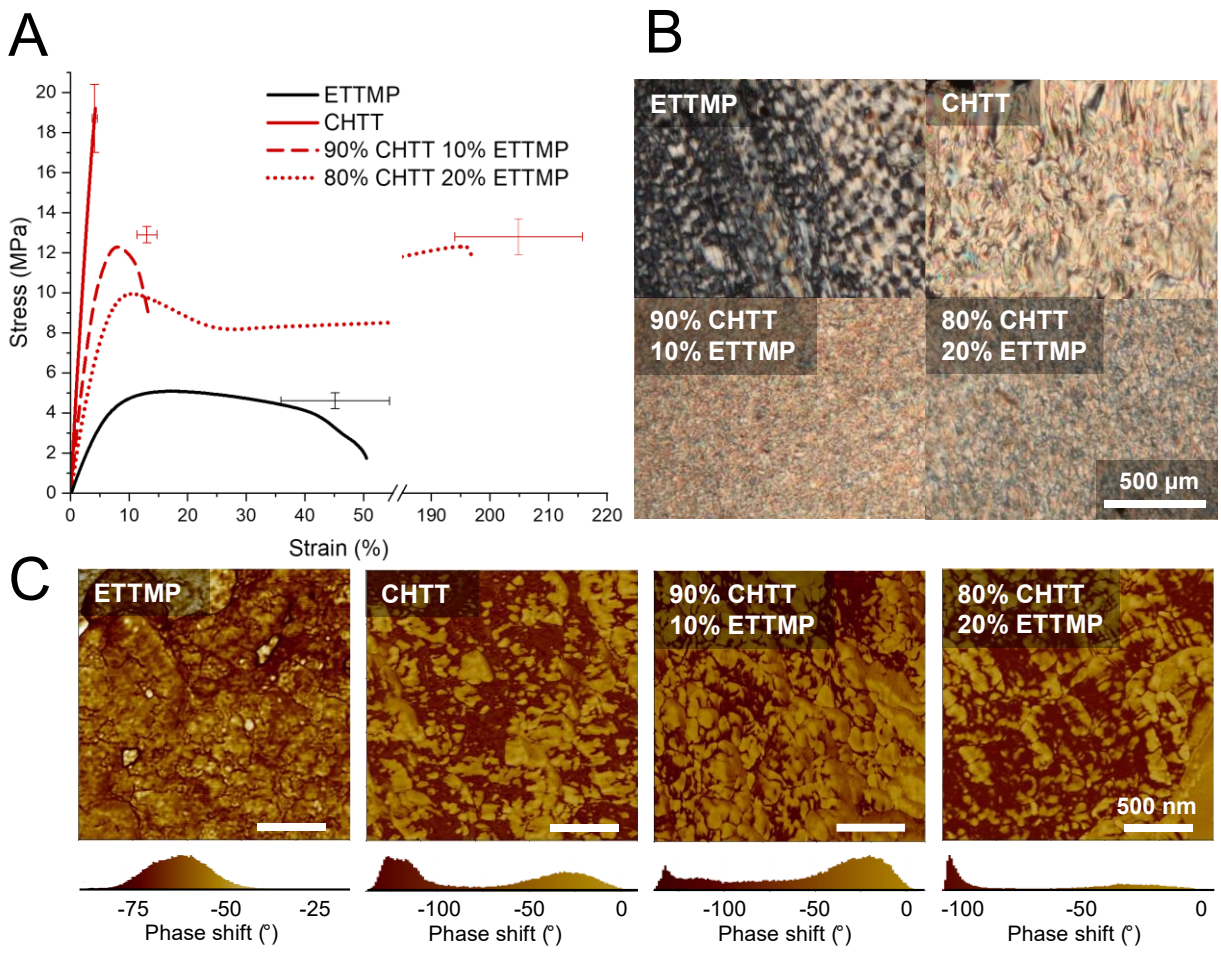

Figure 4: *Mechanical and microstructural characterization of polymers exhibiting the highest degree of crystallinity, derived from LCM and the trithiol comonomers CHTT and ETTMP.* ***A)*** *Representative tensile testing curves of the polymers and corresponding average strength and elongation at break.* ***B)*** *Polarized optical microscopy of 10 µm thick microtome cuts of polymer samples.* ***C)*** *Atomic force microscopy phase images (2x2 µm) and resulting histograms of these areas.*

Additionally, atomic force microscopy (AFM) enhanced by force-distance spectroscopy was conducted on polished surfaces (**Figure 4 C**). Phase imaging allows for a qualitative assessment of material properties (stiffness, viscoelasticity, adhesion or others) across the scanned surface. We observed a strong phase separation between a softer and harder phase for the pure CHTT-containing polymer with little interphase content. By utilizing force-distance spectroscopy and calculating the Young's modulus based on the DMT model,[48] quantitative assessments of local properties can be made. We identified the bright-colored areas as the harder phase, as they display an approximately 60% higher Young's modulus than the dark-colored areas (Supplementary Figure 18).

When the toughener ETTMP is employed to substitute CHTT in concentrations of 10 and 20 mol%, the difference in modulus between soft and hard phases was reduced to 20% and 17%, respectively. An increase of interphase content is observed along with an overall reduction of modulus in both cases.

In comparison, pure ETTMP as a comonomer does not give the characteristic texture of the other measured samples and the monomodal phase shift diagram indicates that no phase separation takes place. This is consistent with the rubbery behavior of the sample observed in DMA and tensile tests.

7 Shape memory behavior

To investigate shape memory behavior, a bulk cured sample from LCM and CHTT was examined. For the quantitative assessment of shape recovery, two key values were required: In an initial assessment the softening temperature, at which the specimen becomes malleable, was determined as 138 °C (Supplementary Figure 20), which also matches the melting point determined via DMA (**Figure 3 C, D**). As intended, the specimen remained in its deformed shape after cooling and recovered its initial shape upon reheating. Additionally, the approximate maximum strain at 138°C was determined to set the elongation limit for shape recovery experiments. After heating the material

above 138 °C and carefully stretching it manually, 74% elongation were achieved before fracture occurred (Supplementary Figure 21).

Based on these key values, quantitative analysis of shape recovery was conducted. For this purpose, the DMA instrument was used to expose a tensile test specimen to programmed cycles of (i) heating to 140 °C (ii) stretching to 50% strain, (iii) cooling to room temperature, (iv) releasing the applied force and (v) reheating to 140 °C without applying external stress (**Figure 5 A**, Supplementary Figure 22). From (iv) the occurring contraction of the specimen allows the calculation of the shape fixity ratio[49], which is the percentage of shape deformation that persists after shape imprinting. (v) is used to calculate the percentage of recovery of the remaining strain. For all cycles except the first, excellent shape recoveries above 96% were achieved. Even more impressively, shape recovery continuously improved and reached numbers above 98% during the final cycles due to the training phenomenon.[49] Throughout all measurements, near-complete shape fixity was achieved (99%) with an average shape recovery of around 97%.

8 3D printing

To access the full potential of the semicrystalline polymer networks, we investigated their processing into arbitrary shapes via 3D printing. We chose the formulation containing 100% CHTT as crosslinker, which led to the highest absolute crystallinity in bulk studies along with the highest tensile strength. A custom-built heated digital light processing (DLP)-based 3D printer was utilized, with which the temperature can be controlled precisely enough to keep the entire formulation in its liquid crystalline state throughout the printing process. In an initial test, we irradiated a droplet of formulation in the heated vat, which causes solidification in its crystalline state to take place after around five seconds (Supplementary Video 1). A subsequently printed resolution test chip (**Figure 5 B**) demonstrates excellent printing resolution after removing the excess formulation by sonication of the specimen in toluene (**Figure 5 C**). Good layer adhesion of macroscopic 3D objects was demonstrated by printing pyramid specimens (**Figure 5 B**).

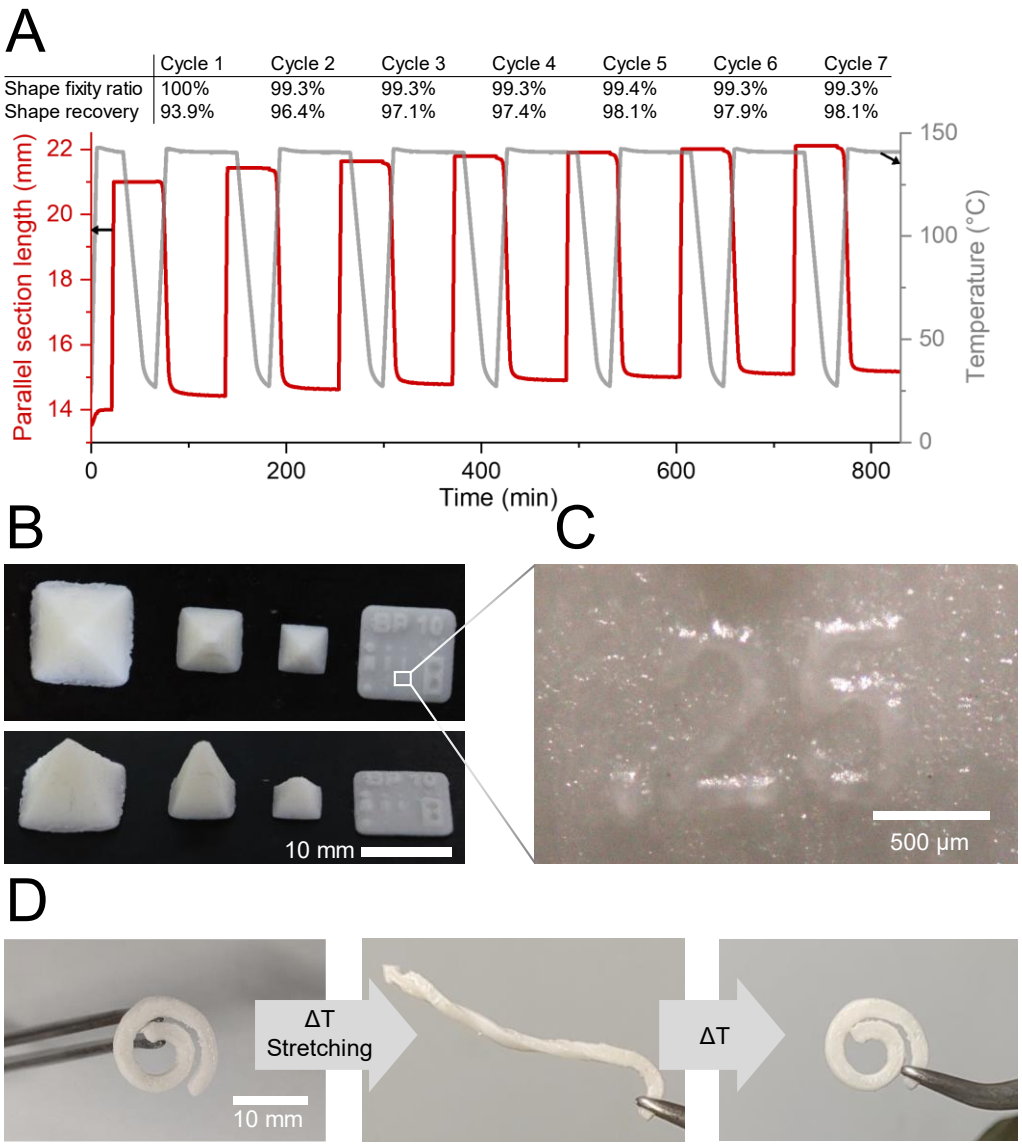

Figure 5: A) *Cyclic shape memory test of bulk-cured polymer cured from monomers LCM and CHTT. In red, the length of the parallel section of the tensile test specimen used in the test is displayed. In grey, the temperature cycles are shown. The numbers above the graph indicate the shape fixity ratio and shape recovery percentages for each cycle.* ***B)*** *Top- and front-view of 3D printed specimens of LCM-CHTT polymer.* ***C)*** *Light microscopy of print resolution test chip depicting ".25" text in well-resolved detail with a dot diameter of 250 µm and font thickness of 125 µm.* ***D)*** *Shape memory behavior of printed part: Upon heating above the crystallite melting point, the sample can be deformed akin to an elastomeric polymer. After cooling, the polymer remains in the deformed shape until it is again heated above the crystallite melting point (138 °C), where it returns to its original printed shape.*

DSC measurements of the printed part confirm their crystallinity, albeit less pronounced (13%) with a broader melting temperature range (Supplementary Figure 19). This could be explained by the faster solidification due to more intense irradiation leading to

complete crosslinking before crystallinity can develop. Further increase in crystallinity may be possible by decreasing the irradiation intensity while increasing the exposure time, which would, however, have a negative impact on the printing speed. To demonstrate that 3D printing can produce the same shape memory effect observed in bulk specimens, a 3D printed spiral was subjected to a shape memory test, in which it was heated and stretched into a straightened shape, which solidified rapidly upon removal of the heat source. Upon reheating, the spiral shape was restored (**Figure 5 D**, Supplementary Video 2). Typically, after 3-4 cycles, the pressure of the tweezers used to hold the specimen in place caused a piece to break off. Nevertheless, the shape recovery process was repeated successfully 20+ times. We attribute this consistently high shape recovery over many cycles to the unique combination of high crosslinking density with high degree of crystallinity in the presented material.

9 Conclusions

Herein, a neat thiol-ene photoclick polymerization from the liquid crystalline phase is demonstrated for the first time as a powerful method to homogeneously incorporate liquid crystalline groups into the main chain of densely crosslinked polymer networks. Tuning the comonomer molecular weight to achieve liquid crystalline preordering enhances the polymer crystallinity and crosslink density, which are typically competing properties. Further comonomer adjustment allows the programming of mechanical properties from those of a stiff, hard thermoset to those of a tough, yielding thermoplastic with over 200% elongation. Micro- and nanostructural analysis indicate phase separation between soft and hard phases as a result of the liquid crystalline preordering, effectively acting as a thermomechanical toughening mechanism. Lastly, we demonstrate 3D printing of one of these materials using the Hot Lithography method, and its potential as a functional, smart material that additionally displays shape memory behavior with a shape imprinting response of over 99% fixity and shape recovery values of above 98% over numerous cycles after an initial acclimatization phase. The high shape recovery

temperature enables a broad application temperature range (0-100°C) without unintended shape recovery.

The expansion of mechanical properties of printable shape-memory polymers from elastomeric to stiff, strong and tough holds great potential in many smart material applications. For example, a pre-programmed shape change of a structural element from one stiff, load bearing shape to a different one could have applications in small, remotely or even autonomously controlled electronic or mechanical devices.

10 Methods

Monomer synthesis and characterization

Detailed synthetic procedures and analysis results are available in the Supplementary Information (Chapter 3).

The precursor to LCM, 4-(5-hexen-1-yl)benzoic acid methyl ester, was synthesized from 6-bromo-1-hexene and 4-chlorobenzoic acid methyl ester according to Fürstner et al.[39] in an iron-catalyzed coupling reaction, which gave the product as a clear oil (35% after distillation). The methyl ester was cleaved under alkaline conditions, which yielded 4-(5-hexen-1-yl)benzoic acid as an off-white solid (94% after recrystallization). The carboxylic acid was then subjected to a Steglich esterification according to Zhang et al.[50] with hydroquinone, yielding LCM as a white powder (58% after recrystallization). The monomer was characterized by ^{1}H- and ^{13}C-NMR, high-resolution mass spectrometry, dynamic scanning calorimetry, polarized optical microscopy and X-ray diffraction (Supplementary Information Chapter 3.1.3).

Formulation preparation and analysis

For all formulations, 0.05 wt% (based on total formulation weight) of the inhibitor pyrogallol was weighed into a brown glass vial, followed by 0.5 mol% (based on terminal double bonds) of photoinitiator TPO. Next, the thiol(s) were added, and the mixture was carefully heated to approximately 50 °C and stirred on a vortex mixer to dissolve the inhibitor and initiator to improve stability and homogeneity of the formulation. Lastly,

LCM was added, and the mixture was heated to approximately 120 °C and fully homogenized using a vortex mixer. An equimolar ratio of thiol and alkene end groups was used in all cases. Monomer purity was not considered for this ratio. Formulation liquid crystallinity was evaluated using a polarized optical light microscope with crossed polarizers (Supplementary Information Chapter 4.1).

Bulk curing

To obtain bulk polymer specimens from the formulations, the formulation components were molten and homogenized as described above and poured into a custom-built heated mold, which allows accurate temperature control (Supplementary Figures 1 and 2). The irradiation protocol was optimized to ensure homogeneous curing from the liquid crystalline state without temperature variation due to evolving polymerization heat. The sample thickness was approximately 2 mm. The mold was preheated to 100 °C and an initial irradion step was conducted for 300 s at 1.5 mW cm^{-2} using a 405 nm LED light source. Afterwards, a second irradiation was employed at 290 mW cm^{-2} for 180 s using a 365 nm LED light source. These irradiation steps were repeated after the specimens were flipped carefully in the mold.

Polymer network analysis

To measure dynamic mechanical analysis (DMA) of bulk cured samples using the heated mold, cuboid samples (DIN EN ISO 6721) were cured as described previously, and sanded to correct any geometric irregularities. Measurements were performed in torsional mode in a temperature range of -50 to 200 °C with a heating rate of 2 °C min^{-1}, a shear strain of 0.1% and a frequency of 1 Hz.

To perform differential scanning calorimetry (DSC), 3-5 mg of the polymer networks were weighed into aluminium DSC crucibles and heated to 200 °C from room temperature, after which the sample was cooled to -90 °C. With this uniformized thermal history, the samples were once again heated to 200 °C. All heating and cooling rates were constant at 10 °C min^{-1}. All reported transition temperatures and enthalpies were taken from the second heating cycle. Crystallinity calculations from obtained enthalpies are described in

depth in the Supplementary Information (Chapter 5.1.1, Chapter 5.2). Polymer networks were either cured in bulk in the heated mold or 3D printed, as stated in each case.

To perform tensile tests, dogbone specimens were cured according to ISO 527 test specimen 5b in bulk in the heated mold. The specimens were sanded to ensure even thickness and clamped into the device, on which the traverse speed was set to 5 mm min^{-1}.

Cryo-microtome cuts were prepared at a thickness of 10 µm at -80 °C with a glass knife and analyzed using polarized optical microscopy as described above.

Atomic force microscopy was conducted on bulk cured polymer specimens utilizing the heated mold. These specimens were embedded in a clear epoxy resin and polished to achieve a smooth surface. Imaging was performed in intermittent (tapping) mode at a scan rate of 0.7 Hz, using an AC160TS cantilever with a spring constant of 26 N m^{-1}, and a tip radius of 7 nm. The phase images were compared with topography images to verify that the observed features were not artifacts of surface unevenness.

Shape memory behavior was analyzed by fastening a tensile test dogbone specimen into a dynamic mechanical analysis device equipped with a tensile test sample bracket. The sample was heated to 140 °C with a heating rate of 20 °C min^{-1} and, after an equilibration period, strained by 50% based on the length of the parallel section of the specimen. The sample was air-cooled to room temperature using a cooling rate of 5 °C min^{-1}. The strain previously applied by the measurement device was removed to test the ensuing contraction of the sample (shape fixity). Next, the sample was heated to 140 °C again with a heating rate of 10 °C min^{-1} under no external stress and held at this temperature for 70 min. The contraction of the sample during this process was recorded and divided by the sample strain after it was allowed to contract to calculate the shape recovery. This process was repeated up to 10 times during one measurement. The equations used to calculate shape fixity and shape recovery are given in the Supplementary Information (Supplementary Equations 3 and 4).

3D printing and post processing

3D printing was performed using a digital light processing printer at a vat temperature of 105 °C and using an LED with its emission maximum centered around 385 nm (Supplementary Figure 4). 50 µm thick layers were exposed for 11 s each with an irradiation intensity of 25 mW cm^{-2}. The vat was coated with formulation for each layer by simply moving the building platform upwards and back down into printing position.

Since the formulation becomes solid at room temperature, post-processing of printed parts requires careful removal of the solid with a suitable solvent by sonication. In the optimized process, specimens were sonicated in toluene for around two minutes at approximately 40 °C.

11 Acknowledgements

We thank Klaudia Hradil, Werner Artner and Berthold Stöger from TU Wien's X-Ray Center (XRC) for conducting the X-ray diffraction experiments, and Edma Gjata for her support with figure design.

12 Data Availability Statement

The data supporting this article have been included as part of the Supplementary Information. Data for this article beyond the scope of the Supplementary Information, including raw data of all presented graphs, are available at TU Wien Research Data at https://doi.org/10.48436/9d7a0-wqh32.

13 References

1 Cacucciolo, V. *et al.* Stretchable pumps for soft machines. *Nature* **572**, 516-519 (2019). https://doi.org:10.1038/s41586-019-1479-6

2 Mishra, A. K., Del Dottore, E., Sadeghi, A., Mondini, A. & Mazzolai, B. SIMBA: Tendon-Driven Modular Continuum Arm with Soft Reconfigurable Gripper. *Frontiers in Robotics and AI* **4** (2017). https://doi.org:10.3389/frobt.2017.00004

3 Zhang, Y. *et al.* Seamless multimaterial 3D liquid-crystalline elastomer actuators for next-generation entirely soft robots. *Science Advances* **6**, eaay8606 (2020). https://doi.org:10.1126/sciadv.aay8606

4 Vinciguerra, M. R. *et al.* Multimaterial Printing of Liquid Crystal Elastomers with Integrated Stretchable Electronics. *ACS Appl Mater Interfaces* **15**, 24777-24787 (2023). https://doi.org:10.1021/acsami.2c23028
5 Kim, H. *et al.* Responsive, 3D Electronics Enabled by Liquid Crystal Elastomer Substrates. *ACS Appl Mater Interfaces* **11**, 19506-19513 (2019). https://doi.org:10.1021/acsami.9b04189
6 Shaha, R. K. *et al.* Biocompatible liquid-crystal elastomers mimic the intervertebral disc. *Journal of the Mechanical Behavior of Biomedical Materials* **107**, 103757 (2020). https://doi.org:10.1016/j.jmbbm.2020.103757
7 Roche, E. T. *et al.* Soft robotic sleeve supports heart function. *Science Translational Medicine* **9**, eaaf3925 (2017). https://doi.org:10.1126/scitranslmed.aaf3925
8 Ferrantini, C. *et al.* Development of Light-Responsive Liquid Crystalline Elastomers to Assist Cardiac Contraction. *Circulation Research* **124**, e44-e54 (2019). https://doi.org:10.1161/CIRCRESAHA.118.313889
9 Guo, H., Terentjev, A., Saed, M. O. & Terentjev, E. M. Momentum transfer on impact damping by liquid crystalline elastomers. *Sci Rep* **13**, 10035 (2023). https://doi.org:10.1038/s41598-023-37215-9
10 Sun, X. *et al.* Light-oriented 3D printing of liquid crystal/photocurable resins and in-situ enhancement of mechanical performance. *Nat Commun* **14**, 6586 (2023). https://doi.org:10.1038/s41467-023-42369-1
11 Hanzon, D. W. *et al.* Adaptable liquid crystal elastomers with transesterification-based bond exchange reactions. *Soft Matter* **14**, 951-960 (2018). https://doi.org:10.1039/c7sm02110k
12 Brannum, M. T. *et al.* Light Control with Liquid Crystalline Elastomers. *Advanced Optical Materials* **7** (2019). https://doi.org:10.1002/adom.201801683
13 Kwon, C., Nam, S., Han, S. H. & Choi, S. S. Optical Characteristics of Stretchable Chiral Liquid Crystal Elastomer under Multiaxial Stretching. *Advanced Functional Materials* **33** (2023). https://doi.org:10.1002/adfm.202304506
14 Xiao, Y. Y., Jiang, Z. C., Tong, X. & Zhao, Y. Biomimetic Locomotion of Electrically Powered "Janus" Soft Robots Using a Liquid Crystal Polymer. *Adv Mater* **31**, e1903452 (2019). https://doi.org:10.1002/adma.201903452
15 He, Q. *et al.* Electrically controlled liquid crystal elastomer–based soft tubular actuator with multimodal actuation. *Science Advances* **5**, eaax5746 (2019). https://doi.org:10.1126/sciadv.aax5746
16 Wu, J. *et al.* Liquid Crystal Elastomer Metamaterials with Giant Biaxial Thermal Shrinkage for Enhancing Skin Regeneration. *Adv Mater* **33**, e2106175 (2021). https://doi.org:10.1002/adma.202106175
17 Ge, S. J. *et al.* A homeotropic main-chain tolane-type liquid crystal elastomer film exhibiting high anisotropic thermal conductivity. *Soft Matter* **13**, 5463-5468 (2017). https://doi.org:10.1039/c7sm01154g

18 Sánchez-Ferrer, A. & Finkelmann, H. Thermal and Mechanical Properties of New Main-Chain Liquid-Crystalline Elastomers. *Molecular Crystals and Liquid Crystals* **508**, 348/[710]-356/[718] (2009). https://doi.org:10.1080/15421400903065861
19 Huang, Y. *et al.* Photocontrollable Elongation Actuation of Liquid Crystal Elastomer Films with Well-Defined Crease Structures. *Adv Mater* **35**, e2304378 (2023). https://doi.org:10.1002/adma.202304378
20 Zhang, M., Pal, A., Lyu, X., Wu, Y. & Sitti, M. Artificial-goosebump-driven microactuation. *Nat Mater* **23**, 560-569 (2024). https://doi.org:10.1038/s41563-024-01810-6
21 Hisano, K. *et al.* Mechano-Optical Sensors Fabricated with Multilayered Liquid Crystal Elastomers Exhibiting Tunable Deformation Recovery. *Advanced Functional Materials* **31** (2021). https://doi.org:10.1002/adfm.202104702
22 Barnes, M. *et al.* Reactive 3D Printing of Shape-Programmable Liquid Crystal Elastomer Actuators. *ACS Appl Mater Interfaces* **12**, 28692-28699 (2020). https://doi.org:10.1021/acsami.0c07331
23 Lopez-Valdeolivas, M., Liu, D., Broer, D. J. & Sanchez-Somolinos, C. 4D Printed Actuators with Soft-Robotic Functions. *Macromol Rapid Commun* **39** (2018). https://doi.org:10.1002/marc.201700710
24 Herbert, K. M. *et al.* Synthesis and alignment of liquid crystalline elastomers. *Nature Reviews Materials* **7**, 23-38 (2021). https://doi.org:10.1038/s41578-021-00359-z
25 Javed, M. *et al.* Programmable Shape Change in Semicrystalline Liquid Crystal Elastomers. *ACS Appl Mater Interfaces* **14**, 35087-35096 (2022). https://doi.org:10.1021/acsami.2c07533
26 Westbrook, K. K. *et al.* Two-way reversible shape memory effects in a free-standing polymer composite. *Smart Materials and Structures* **20** (2011). https://doi.org:10.1088/0964-1726/20/6/065010
27 Behl, M. & Lendlein, A. Actively moving polymers. *Soft Matter* **3**, 58-67 (2006). https://doi.org:10.1039/b610611k
28 Hebner, T. S., Korner, K., Bowman, C. N., Bhattacharya, K. & White, T. J. Leaping liquid crystal elastomers. *Science Advances* **9**, eade1320 https://doi.org:10.1126/sciadv.ade1320
29 Martinez, A. M., McBride, M. K., White, T. J. & Bowman, C. N. Reconfigurable and Spatially Programmable Chameleon Skin-Like Material Utilizing Light Responsive Covalent Adaptable Cholesteric Liquid Crystal Elastomers. *Advanced Functional Materials* (2020). https://doi.org:10.1002/adfm.202003150
30 Hsu, L.-Y. *et al.* Alignment and actuation of liquid crystals via 3D confinement and two-photon laser printing. *Science Advances* **10**, eadq2597 https://doi.org:10.1126/sciadv.adq2597

31 Fleischmann, E.-K., Forst, F. R., Köder, K., Kapernaum, N. & Zentel, R. Microactuators from a main-chain liquid crystalline elastomer via thiol–ene "click" chemistry. *Journal of Materials Chemistry C* **1** (2013). https://doi.org:10.1039/c3tc30272e

32 Liu, M., Yin, L. & Zhao, Y. Effect of Spacer and Mesogen in Side-Chain Liquid Crystal Elastomer Structure on Reversible Actuation Behavior. *Macromolecules* **56**, 9431-9442 (2023). https://doi.org:10.1021/acs.macromol.3c01310

33 Fowler, H. E., Pearl, H. M., Hoang, J. D. & White, T. J. Liquid Crystal Elastomers Prepared by Thiol–Ene Photopolymerization Amenable to Surface-Enforced Alignment. *Macromolecules* **57**, 2619-2627 (2024). https://doi.org:10.1021/acs.macromol.3c02291

34 Ware, T. H., Perry, Z. P., Middleton, C. M., Iacono, S. T. & White, T. J. Programmable Liquid Crystal Elastomers Prepared by Thiol–Ene Photopolymerization. *ACS Macro Letters* **4**, 942-946 (2015). https://doi.org:10.1021/acsmacrolett.5b00511

35 Ware, T. H. & White, T. J. Programmed liquid crystal elastomers with tunable actuation strain. *Polymer Chemistry* **6**, 4835-4844 (2015). https://doi.org:10.1039/c5py00640f

36 Ohm, C., Brehmer, M. & Zentel, R. Liquid crystalline elastomers as actuators and sensors. *Adv Mater* **22**, 3366-3387 (2010). https://doi.org:10.1002/adma.200904059

37 Gu, Y., Zhao, J. & Johnson, J. A. Polymer Networks: From Plastics and Gels to Porous Frameworks. *Angew Chem Int Ed Engl* **59**, 5022-5049 (2020). https://doi.org:10.1002/anie.201902900

38 Ahmadi, M., Ehrmann, K., Koch, T., Liska, R. & Stampfl, J. From Unregulated Networks to Designed Microstructures: Introducing Heterogeneity at Different Length Scales in Photopolymers for Additive Manufacturing. *Chem Rev* **124**, 3978-4020 (2024). https://doi.org:10.1021/acs.chemrev.3c00570

39 Fuerstner, A., Leitner, A., Mendez, M. & Krause, H. Iron-Catalyzed Cross-Coupling Reactions. *J. Am. Chem. Soc.* **124**, 13856-13863 (2002). https://doi.org:10.1021/ja027190t

40 Sannasi, V., Jose, T. P. & Jeyakumar, D. Synthesis and optical properties of poly(2,7-(9,9-dihexylfluorene)-3,3′(4,4′-dialkoxybiphenyl)). *Designed Monomers and Polymers* **18**, 51-63 (2014). https://doi.org:10.1080/15685551.2014.947553

41 Kidowaki, M., Moriyama, M., Wada, M. & Tamaoki, N. Molecular Mechanism of Anomalous Increase in the Helical Pitch of Cholesteric Liquid Crystals Induced by Achiral Dopants. *J. Phys. Chem. B* **107**, 12054-12061 (2003). https://doi.org:10.1021/jp034916e

42 Watanabe, G. & Tabe, Y. Tilted and Non-tilted Liquid Crystalline Langmuir Monolayers: Analogy to Bulk Smectic Phases. *Journal of the Physical Society of Japan* **76** (2007). https://doi.org:10.1143/jpsj.76.094602

43 Hikmet, R. A. M. & Lub, J. Anisotropic networks and gels obtained by photopolymerisation in the liquid crystalline state: Synthesis and applications.

Progress in Polymer Science **21**, 1165-1209 (1996). https://doi.org:10.1016/S0079-6700(96)00017-2

44 Vyakaranam, K., Barbour, J. B. & Michl, J. Li+-Catalyzed Radical Polymerization of Simple Terminal Alkenes. *Journal of the American Chemical Society* **128**, 5610-5611 (2006). https://doi.org:10.1021/ja060087+

45 Li, Y. *et al.* Liquid crystalline networks based on photo-initiated thiol-ene click chemistry. *Soft Matter* (2019). https://doi.org:10.1039/c9sm01818b

46 Wang, Y., Liu, J. & Yang, S. Multi-functional liquid crystal elastomer composites. *Applied Physics Reviews* **9** (2022). https://doi.org:10.1063/5.0075471

47 Chen, M. *et al.* Recent Advances in 4D Printing of Liquid Crystal Elastomers. *Adv Mater* **35**, e2209566 (2023). https://doi.org:10.1002/adma.202209566

48 Derjaguin, B. V., Muller, V. M. & Toporov, Y. P. Effect of contact deformations on the adhesion of particles. *Journal of Colloid and Interface Science* **53**, 314-326 (1975). https://doi.org:10.1016/0021-9797(75)90018-1

49 Defize, T. *et al.* Thermoreversibly crosslinked poly(epsilon-caprolactone) as recyclable shape-memory polymer network. *Macromol Rapid Commun* **32**, 1264-1269 (2011). https://doi.org:10.1002/marc.201100250

50 Zhang, G. Y., Lu, H. B. & Xu, W. B. Synthesis and Application of a Novel Liquid Crystal Monomer 1,4-di-[4-(3-acryloyloxyhexyloxy)benzoyloxy]-2-methyl Benzene. *Advanced Materials Research* **875-877**, 3-8 (2014). https://doi.org:10.4028/www.scientific.net/AMR.875-877.3